tive version in the construction of natural products. To illustrate, the carbon skeleton of the sesquiterpene natural products, a large family with many biologically active members in both enantiomeric series, was targeted (*18*). The retrosynthesis involved constructing the polycyclic core of these molecules by using the TADA of silicon-containing macrocyclic ketone **8** (Fig. 4A) (*19*). Postcyclization, straightforward synthetic manipulations of the tricyclic product **9** would provide access to various members of this interesting natural product class. Construction of such a decalin framework using traditional Diels-Alder partners that lack a macrocyclic tether is problematic because of the development of severe *syn* pentane-like interactions between the *gem*-dimethyl group and the methyl group of the dienenophile in the transition state (*20*).

Synthesis of the desired TADA substrate was achieved in eight steps from known ketoaldehyde **10** (Fig. 4B) (*21*). Silylation of alcohol **11** was followed by macrocyclization via diene-ene ring-closing metathesis using the Grubbs first-generation ruthenium catalyst, which proceeded in excellent conversion and with good selectivity for the *E,E* diene product **8** (*22*). Gratifyingly, exposure of this macrocycle to catalyst **3f** resulted in complete conversion of the *E,E* isomer to provide the desired TADA product **9** in >20:1 dr. Tamao oxidation of the crude reaction mixture (*23*), followed by oxidative cleavage of the resulting diastereomeric mixture of hemiketals, provided lactone **12** in 83% ee. This intermediate, which could potentially serve as a precursor to a number of sesquiterpene targets, was elaborated in three steps to a representative natural product, 11,12-diacetoxydrimane (*24*). In addition to providing a concise, enantioselective route to these terpene targets, the strategic use of a temporary transannular tether may constitute an important approach for dealing with difficult bond constructions in a variety of systems.

The successful application of a chiral catalyst to transannnular reactions is thus not only possible but is seen to be remarkably general across a broad range of macrocyclic substrates. This strategy should allow stereocontrolled assembly of polycyclic molecular architectures with unparalleled efficiency and elegance.

References and Notes

1. D. M. Hodgson *et al.*, *J. Chem. Soc. Perkin Trans. 1* 2151 (1998).
2. D. M. Hodgson, L. A. Robinson, *Chem. Commun.* 309 (1999).
3. D. M. Hodgson, I. D. Cameron, *Org. Lett.* **3**, 441 (2001).
4. O. Knopff, J. Kuhne, C. Fehr, *Angew. Chem. Int. Ed.* **46**, 1307 (2007).
5. M. Inoue *et al.*, *J. Org. Chem.* **72**, 3065 (2007).
6. P. Deslongchamps, *Pure Appl. Chem.* **64**, 1831 (1992).
7. P. Deslongchamps, *Aldrichchimica Acta* **24**, 43 (1991).
8. E. Marsault, A. Toró, P. Nowak, P. Deslongchamps, *Tetrahedron* **57**, 4243 (2001).
9. D. A. Evans, J. S. Johnson, in *Comprehensive Asymetric Catalysis*, E. N. Jacobsen, A. Pfaltz, H. Yamamoto, Eds. (Springer-Verlag, Berlin, 1999), vol. 3, ch. 33.1.
10. Materials and methods are available on *Science* Online.
11. E. J. Corey, T. Shibata, T. W. Lee, *J. Am. Chem. Soc.* **124**, 3808 (2002).
12. D. H. Ryu, E. J. Corey, *J. Am. Chem. Soc.* **125**, 6388 (2003).
13. G. Zhou, Q.-Y. Hu, E. J. Corey, *Org. Lett.* **5**, 3979 (2003).
14. S. Masamune, W. Choi, J. S. Petersen, L. R. Sita, *Angew. Chem. Int. Ed.* **24**, 1 (1985).
15. D. J. Witter, J. C. Vederas, *J. Org. Chem.* **61**, 2613 (1996).
16. M. D. Burke, S. L. Schreiber, *Angew. Chem. Int. Ed.* **43**, 46 (2004).
17. A. G. Myers *et al.*, *J. Am. Chem. Soc.* **119**, 6496 (1997).
18. B. M. Fraga, *Nat. Prod. Rep.* **23**, 943 (2006); and references therein.
19. G. Stork, T. Y. Chan, G. A. Breault, *J. Am. Chem. Soc.* **114**, 7578 (1992).
20. For related examples of utilizing a TADA, see (*8*).
21. M. Negi, G. V. Subbaraju, M. S. Manhas, A. K. Bose, *Enzyme Microb. Technol.* **15**, 483 (1993).
22. K. Lu *et al.*, *Org. Lett*. **8**, 1193 (2006); and references therein.
23. K. Tamao, N. Ishida, M. Kumada, *J. Org. Chem.* **48**, 2120 (1983).
24. A. Montagnac, M.-T. Martin, C. Debitus, M. Pais, *J. Nat. Prod.* **59**, 866 (1996).

25. Financial support was provided by the NIH (GM-59316). E.P.B. is the recipient of a predoctoral fellowship from NSF and an American Chemical Society Division of Organic Chemistry fellowship sponsored by Schering-Plough.

Supporting Online Material

www.sciencemag.org/cgi/content/full/317/5845/1736/DC1
Materials and Methods
Figs. S1 to S13
References

25 June 2007; accepted 6 August 2007
10.1126/science.1146939

Spin Transition Zone in Earth's Lower Mantle

Jung-Fu Lin,[1] György Vankó,[2,3] Steven D. Jacobsen,[4] Valentin Iota,[1] Viktor V. Struzhkin,[5] Vitali B. Prakapenka,[6] Alexei Kuznetsov,[6] Choong-Shik Yoo[1]*

Mineral properties in Earth's lower mantle are affected by iron electronic states, but representative pressures and temperatures have not yet been probed. Spin states of iron in lower-mantle ferropericlase have been measured up to 95 gigapascals and 2000 kelvin with x-ray emission in a laser-heated diamond cell. A gradual spin transition of iron occurs over a pressure-temperature range extending from about 1000 kilometers in depth and 1900 kelvin to 2200 kilometers and 2300 kelvin in the lower mantle. Because low-spin ferropericlase exhibits higher density and faster sound velocities relative to the high-spin ferropericlase, the observed increase in low-spin (Mg,Fe)O at mid-lower mantle conditions would manifest seismically as a lower-mantle spin transition zone characterized by a steeper-than-normal density gradient.

Electronic spin-pairing transitions of iron and associated effects on the physical properties of host phases have been reported in lower-mantle minerals, including ferropericlase, silicate perovskite, and possibly in post-silicate perovskite at high pressures, but so far only at room temperature experimentally (*1*–*12*). These mineral physics studies have prompted geophysicists and geodynamicists to reevaluate the state of the lower mantle and, in particular, the possible sources of seismic (*13*–*15*) and chemical (*16*, *17*) heterogeneities, as well as the thermal stability of massive upwellings (*18*, *19*) in terms of spin-pairing phenomena. Changes in the electronic structure of iron are thought to promote partitioning of iron into ferropericlase relative to perovskite (*1*), although experimental evidence is lacking under lower mantle conditions (*6*, *11*, *16*, *17*). Recent theoretical calculations predict that the spin transition of Fe^{2+} in ferropericlase, $(Mg_{1-x}Fe_x)O$ ($x < 0.2$), would occur continuously over an extended pressure range—and thus would be more accurately referred to as a spin crossover—under the pressure-temperature conditions of the lower mantle (*6*, *11*). In this case, the associated effects would be gradual and therefore less likely to permit seismological detection. Because the Earth's lower mantle varies in pressure from 22 to 140 GPa and in temperature from 1800 K to 4000 K (*20*), experimental determination of the simultaneous pressure-temperature effect on the spin transitions of lower-mantle phases is essential.

We have studied the electronic spin states of iron in ferropericlase $[(Mg_{0.75},Fe_{0.25})O]$ and its crystal structure under relevant lower-mantle conditions using x-ray emission spectroscopy (XES) and x-ray diffraction with a laser-heated diamond anvil cell (LHDAC) (*5*, *21*–*23*). The spin states of iron in $(Mg_{0.75},Fe_{0.25})O$ at high pressures and temperatures were probed by in situ XES in a

[1]Lawrence Livermore National Laboratory (LLNL), 7000 East Avenue, Livermore, CA 94550, USA. [2]KFKI Research Institute for Particle and Nuclear Physics, Post Office Box 49, H-1525 Budapest, Hungary. [3]European Synchrotron Radiation Facility, Boîte Postal 220 F-38043, Grenoble Cedex 9, France. [4]Department of Earth and Planetary Sciences, Northwestern University, Evanston, IL 60208, USA. [5]Geophysical Laboratory, Carnegie Institution of Washington, 5251 Broad Branch Road, NW, Washington, DC 20015, USA. [6]Consortium for Advanced Radiation Sources, University of Chicago, Chicago, IL 60637, USA.

*Present address: Department of Chemistry and Institute for Shock Physics, Washington State University, Pullman, WA 99164, USA.

LHDAC. The samples were preoriented <110> crystal plates (*5*) or polycrystalline (*9*) samples of $(Mg_{0.75},Fe_{0.25})O$ composition measuring ~12 μm thick and 70 μm in diameter. Samples were loaded into diamond cells with Be gaskets and boron or cubic BN gasket inserts. Dried NaCl layers acted as thermal insulators between the sample and diamond anvils, as well as the pressure medium and the pressure calibrant (*24*).

A Rowland circle spectrometer with 1-m diameter in the vertical scattering geometry was configured around the double-sided laser-heating system at the GeoSoilEnviro Consortium for Advanced Radiation Sources (GSECARS) sector of the Advanced Photon Source (APS), Argonne National Laboratory (ANL) for XES of iron in the sample under high pressures and temperatures (*5*, *21*). A monochromatic x-ray beam of 14 keV was focused down to ~5 μm vertically and horizontally at the sample position, and a near-infrared laser beam 25 μm in diameter at the sample position was used to heat the sample from both sides of the DAC. The Fe Kβ emission spectra were collected by a silicon detector through the Be gasket and a Si (333) analyzer in the Rowland circle geometry. During the laser-heating experiments, the energy of the monochromatic x-ray was adjusted to higher energy to allow x-ray diffraction measurements with an image plate (MAR345). The details of the experimental set-up and sample synthesis are reported in supporting online material (*22*).

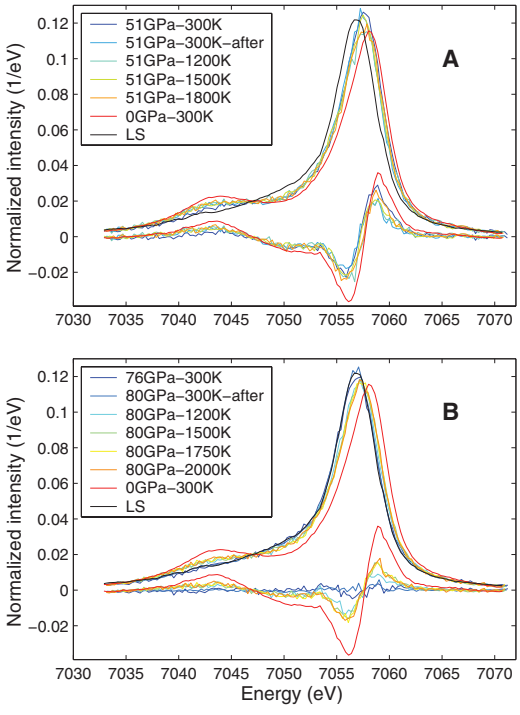

Fig. 1. Representative x-ray emission spectra of Fe Kβ collected from ferropericlase-$(Mg_{0.75},Fe_{0.25})O$ at high pressures and temperatures. (**A**) 51 GPa and high temperatures; (**B**) 80 GPa and high temperatures. High-quality XES spectra collected at ambient pressure and 80 GPa are used as references for the IAD analysis (*23*) of the high-spin and low-spin states, respectively. Differences from the low-spin line shape, shown below the spectra, are used to derive the ratio of the high-spin to low-spin states in the sample. An energy shift of ~1.6 eV in the main emission peak (Kβ) can also be seen across the spin transition.

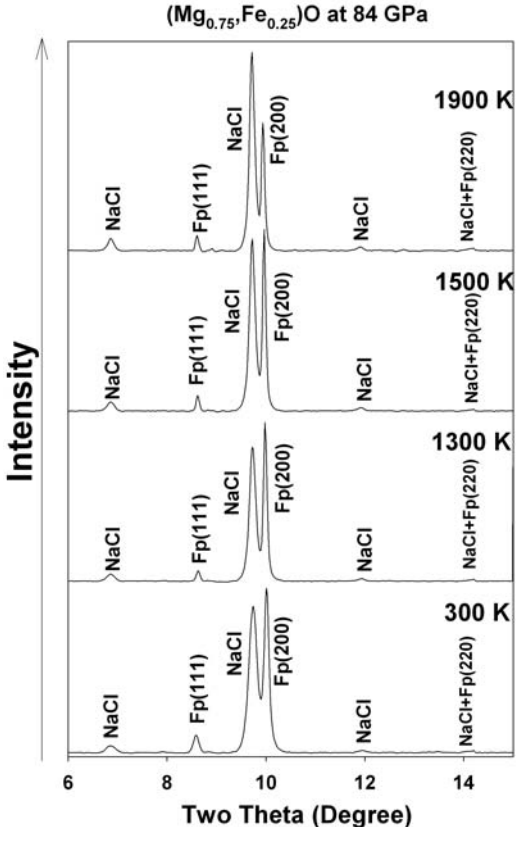

Fig. 2. Representative angle-dispersive x-ray diffraction patterns of $(Mg_{0.75},Fe_{0.25})O$ at ~84 GPa and high temperatures collected from a laser-heated diamond cell. A monochromatic beam of 0.3344 Å in wavelength was used as the x-ray source, and the diffracted x-rays were collected by an image plate (MAR345). The diffraction patterns were integrated with the FIT2D program, and the backgrounds were subtracted for clarity. $(Mg_{0.75},Fe_{0.25})O$ is stable in the B1 structure up to 1900 K and remains in the B1 structure after hours of laser heating (*26*). Fp, $(Mg_{0.75},Fe_{0.25})O$; NaCl, thermal insulator in the B2 structure. Temperature uncertainties in the experiments were approximately 100 to 150 K. Optical observation of the laser-heated sample shows no evidence of a phase separation.

The XES spectra of the Fe Kβ fluorescence lines in $(Mg_{0.75},Fe_{0.25})O$ were collected up to 95 GPa and 2000 K, and x-ray diffraction patterns were collected from some of the samples before, during, and after laser heating at high pressures (Figs. 1 and 2). To quantitatively derive the 3*d* spin momentum and the ratio of the high-spin and low-spin states, the XES spectra were analyzed using the line-shape analysis by integrating the absolute values of the difference spectra and comparing these integrals with that obtained on references [integrated absolute difference (IAD) analysis] (Fig. 1 and figs. S1 and S2) (*23*). The IAD analysis uses the information of the full Fe Kβ spectrum and is model independent. It has been shown that the derived IAD values linearly correlate with the spin momentum at the transition between two spin states and provide a reliable method for determining the ratio of the high-spin and low-spin states in the sample (*23*).

The derived fractions of the high-spin state were used to construct the spin-crossover phase diagram of iron in $(Mg_{0.75},Fe_{0.25})O$ up to 95 GPa and 2000 K (Fig. 3). Whereas the XES results reveal an electronic spin crossover with a mixed population of high-spin and low-spin states of iron in ferropericlase at high pressures and temperatures, x-ray diffraction patterns show that the $(Mg_{0.75},Fe_{0.25})O$ sample is stable in the B1 structure before, during, and after the experiments up to 95 GPa and 2000 K (Fig. 2 and fig. S3) (*25*, *26*). High temperatures do not significantly affect the fraction of the high-spin state below 50 GPa and above 95 GPa, but much stronger temperature effects on the spin crossover are observed from ~50 to 90 GPa. The observed spin crossover is found to be readily reversible in temperatures and cannot be simply explained as the result of sluggish transition and kinetics. The spin-crossover zone clearly widens with increasing temperatures at high pressures (Fig. 3). Although previous high-pressure and room-temperature experiments showed that low-spin and high-spin states have characteristic physical properties, such as volume, incompressibility, and sound velocities, and can be categorized as two distinct phases, high-spin ferropericlase and low-spin ferropericlase (*5*, *7*, *9*),

the spin crossover in the ferropericlase observed in our current XES and diffraction experiments likely involves a mixed population of high-spin and low-spin states in the same crystal structure, an isosymmetric transition involving the substitution of low-spin ions for high-spin ions without change in the structure of the host (*6*, *11*).

Comparison with the model geotherm of the Earth's lower mantle (*20*) indicates that the high-spin to low-spin crossover of iron likely occurs from the middle part to the lower part of the lower mantle from ~1000 km in depth and 1900 K to ~2200 km and 2300 K, and that the low-spin ferropericlase with the B1 structure exists in the lower mantle, that is, at depths below ~2200 km. The observed width of the spin crossover in ferropericlase is much narrower than that predicted by the existing theoretical models (*6*, *11*). Although the temperature effect on the spin transitions in the silicate perovskite and post-perovskite is yet to be studied (*2*–*4*, *8*, *12*), we propose that this spin-crossover phenomenon should also occur in silicate perovskite because it is subject to similar thermal energy in the lower mantle as that required to overcome the spin-pairing energy.

The spin crossover of iron in the lower-mantle phases substantially affects its implications for the geophysics and geodynamics of Earth's lower mantle. The continuous nature of the spin crossover observed here explains why no significant change in iron partitioning between ferropericlase and perovskite has been observed in recent high pressure-temperature experiments with a pyrolitic and olivine composition (*16*, *17*), as opposed to a proposed dramatic change in partitioning and chemical layering in the lower mantle (*1*, *2*). Because the low-spin ferropericlase exhibits relatively high density (*5*, *11*), fast sound velocities (*5*, *9*), and lower radiative thermal conductivity (*7*) than the high-spin ferropericlase, the spin crossover in ferropericlase would result in continuously enhanced density and reduced radiative thermal conductivity of ferropericlase from the middle part to the lower part of the lower mantle. However, slowing in sound velocities and lowering in pressure derivatives of the sound velocities are expected within the transition region (*9*). The observed increase of the low-spin (Mg,Fe)O at the mid-lower mantle conditions would manifest seismically as a lower-mantle spin transition zone (STZ), characterized by a steeper-than-normal density gradient between ~1000 km and 2200 km in depth (*13*–*15*) (Fig. 4). Spin transition may therefore account for some of the seismic wave heterogeneity in that region, and the existence of the low-spin (Mg,Fe)O at the lowermost mantle conditions may affect the thermal stability of the mantle upwellings (*18*, *19*).

Because the spin crossover of iron occurs in the lower-mantle minerals such as ferropericlase at high pressures and temperatures, the thermal compression curves and sound velocities of the lower-mantle minerals will be continuously influenced by the ratio of the high-spin and low-spin states along the lower-mantle geotherm (Figs. 3 and 4). This renders the use of the classical equations of state with lattice finite strain theory unreliable for modeling the density and sound velocity behavior across the spin crossover (*24*, *27*–*29*). For example, a density increase of ~3 to 4% is observed across the high-spin to low-spin transition in ferropericlase at ~50 GPa (*5*, *11*, *22*). Using a pyrolite lower-mantle composition model (*29*, *30*) with ~33% of ferropericlase and assuming a similar thermal compression behavior in high-spin/low-spin (Mg,Fe)O with various iron content (*22*, *31*, *32*), we predict the spin crossover of iron in (Mg,Fe)O would result in a density difference of ~1% between the extrapolated high-spin and low-spin density profiles, affecting our understanding of the lower-mantle chemistry. Such density increase is equivalent to the addition of ~5.0% FeO into MgO in ferropericlase (*32*) and may be further enhanced if the stiffer low-spin ferropericlase (*5*) exhibits less thermal expansion than that extrapolated using the thermal equation of state of the high-spin ferropericlase (*31*). Therefore, knowledge of the ratio of the high-spin to low-spin states in ferropericlase as well as in the silicate perovskite and post-perovskite is essential to evaluate reliably the composition, geophysics, and dynamics of Earth's lower mantle.

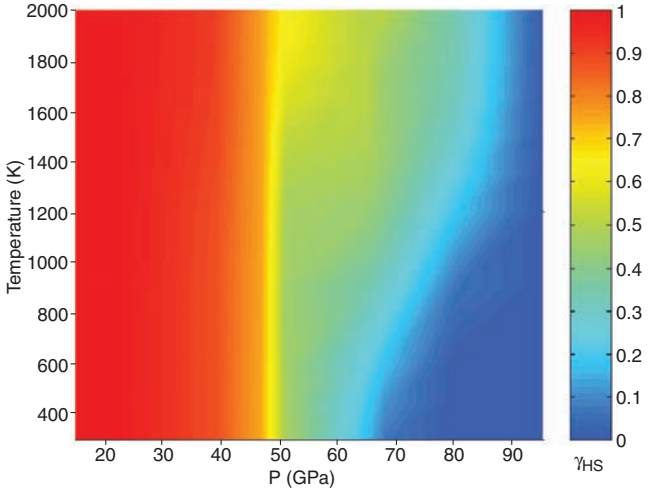

Fig. 3. Isosymmetric spin crossover of Fe^{2+} in $(Mg_{0.75}, Fe_{0.25})O$. The phase diagram is constructed from the interpolation and extrapolation of the derived fractions of the high-spin state in the sample (fig. S2). Colors in the vertical column on the right represent fractions of the high-spin iron, γ_{HS}, in $(Mg_{0.75},Fe_{0.25})O$.

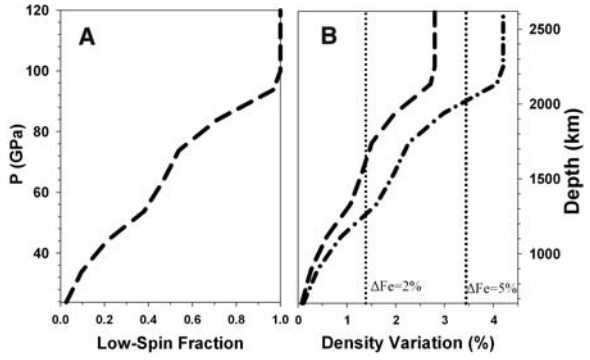

Fig. 4. Derived fractions of the low-spin ferropericlase (**A**) and density variation (**B**) along a model lower-mantle geotherm (*20*). Fraction of the low-spin ferropericlase is derived from an extrapolation of the experimental data in Fig. 3. Density variations in ferropericlase across the spin-crossover region assume that the density varies linearly with the fraction of the low-spin iron (*22*). Dashed line and dash-dotted line represent derived density variations using maximum variations of 2.8% and 4.2% across the spin-crossover region from evaluation of recent experimental (*5*) and theoretical (*11*) data, respectively. Vertical bars represent the density variations caused by 2% and 5% perturbation of total iron content in ferropericlase, respectively, at ambient conditions (*32*).

References and Notes

1. J. Badro *et al.*, *Science* **300**, 789 (2003).
2. J. Badro *et al.*, *Science* **305**, 383 (2004).
3. J. Li *et al.*, *Proc. Natl. Acad. Sci. U.S.A.* **101**, 14027 (2004).
4. J. M. Jackson *et al.*, *Am. Miner.* **90**, 199 (2005).
5. J. F. Lin *et al.*, *Nature* **436**, 377 (2005).
6. W. Sturhahn, J. M. Jackson, J. F. Lin, *Geophys. Res. Lett.* **32**, L12307 (2005).
7. A. F. Goncharov, V. V. Struzhkin, S. D. Jacobsen, *Science* **312**, 1205 (2006).
8. A. M. Hofmeister, *Earth Planet. Sci. Lett.* **243**, 44 (2006).
9. J. F. Lin *et al.*, *Geophys. Res. Lett.* **33**, L22304 (2006).
10. K. Persson, A. Bengtson, G. Ceder, D. Morgan, *Geophys. Res. Lett.* **33**, L16306 (2006).
11. T. Tsuchiya, R. M. Wentzcovitch, C. R. S. da Silva, S. de Gironcoli, *Phys. Rev. Lett.* **96**, 198501 (2006).
12. F. Zhang, A. R. Oganov, *Earth Planet. Sci. Lett.* **249**, 436 (2006).
13. L. H. Kellogg, B. H. Hager, R. D. van der Hilst, *Science* **283**, 1881 (1999).
14. R. D. van der Hilst, H. Kárason, *Science* **283**, 1885 (1999).
15. J. Trampert, F. Deschamps, J. Resovsky, D. Yuen, *Science* **306**, 853 (2004).
16. Y. Kobayashi *et al.*, *Geophys. Res. Lett.* **32**, L19302 (2005).
17. M. Murakami, K. Hirose, N. Sata, Y. Ohishi, *Geophys. Res. Lett.* **32**, L03304 (2005).

18. C. Matyska, D. A. Yuen, *Earth Planet. Sci. Lett.* **154**, 196 (2006).
19. J. B. Naliboff, L. H. Kellogg, *Geophys. Res. Lett.* **33**, L12S09 (2006).
20. J. M. Brown, T. J. Shankland, *Geophys. J. R. Astr. Soc.* **66**, 579 (1981).
21. J. F. Lin *et al.*, *J. Synchrotron Rad* **12**, 637 (2005).
22. Materials and methods are available as supporting material on *Science* Online.
23. G. Vankó *et al.*, *J. Phys. Chem. B* **110**, 11647 (2006).
24. F. Birch, *J. Geophys. Res.* **91**, 4949 (1986).
25. L. S. Dubrovinsky *et al.*, *Science* **289**, 430 (2000).
26. J. F. Lin *et al.*, *Proc. Natl. Acad. Sci. U.S.A.* **100**, 4405 (2003).
27. G. F. Davies, A. M. Dziewonski, *Phys. Earth Planet. Int.* **10**, 336 (1975).
28. T. S. Duffy, D. L. Anderson, *J. Geophys. Res.* **94**, 1895 (1989).
29. E. Mattern, J. Matas, Y. Ricard, J. Bass, *Geophys. J. Int.* **160**, 973 (2005).
30. A. E. Ringwood, *J. Geol.* **90**, 611 (1982).
31. W. van Westrenen *et al.*, *Phys. Earth Planet. Int.* **151**, 163 (2005).
32. S. D. Jacobsen *et al.*, *J. Geophys. Res.* **107**, 2037 (2002).
33. We acknowledge GSECARS, APS, and ANL for the use of the synchrotron and laser facilities and the High Pressure Collaborative Access Team for the use of the ruby system. We thank F. de Groot, J.-P. Rueff, W. Sturhahn, T. Tsuchiya, and W. J. Evans for helpful discussions and G. Shen, M. Hu, and K. Visbeck for their assistance in the experiments. Use of the APS was supported by U.S. Department of Energy (DOE), Office of Science, Basic Energy Sciences, under contract DE-AC02-06CH11357. GSECARS is supported by NSF Earth Sciences (EAR-0622171) and DOE Geosciences (DE-FG02-94ER14466). This work at LLNL was performed under the auspices of the U.S. DOE by University of California and LLNL under contract W-7405-Eng-48. J.-F.L. is also supported by the Lawrence Livermore Fellowship. S.D.J. acknowledges financial support from NSF/EAR 0721449, and V.V.S. acknowledges financial support from DOE.

Supporting Online Material

www.sciencemag.org/cgi/content/full/317/5845/1740/DC1
Materials and Methods
Figs. S1 to S3
References

11 May 2007; accepted 24 July 2007
10.1126/science.1144997

The Primitive Wrist of *Homo floresiensis* and Its Implications for Hominin Evolution

Matthew W. Tocheri,[1]* Caley M. Orr,[2,3] Susan G. Larson,[4] Thomas Sutikna,[5] Jatmiko,[5] E. Wahyu Saptomo,[5] Rokus Awe Due,[5] Tony Djubiantono,[5] Michael J. Morwood,[6] William L. Jungers[4]

Whether the Late Pleistocene hominin fossils from Flores, Indonesia, represent a new species, *Homo floresiensis*, or pathological modern humans has been debated. Analysis of three wrist bones from the holotype specimen (LB1) shows that it retains wrist morphology that is primitive for the African ape-human clade. In contrast, Neandertals and modern humans share derived wrist morphology that forms during embryogenesis, which diminishes the probability that pathology could result in the normal primitive state. This evidence indicates that LB1 is not a modern human with an undiagnosed pathology or growth defect; rather, it represents a species descended from a hominin ancestor that branched off before the origin of the clade that includes modern humans, Neandertals, and their last common ancestor.

The debate over the affinity of the Late Pleistocene hominin fossils from the island of Flores has focused primarily on the craniodental remains of the first specimen (LB1) recovered from Liang Bua cave (*1*–*6*). LB1 is the holotype specimen of a new species, *Homo floresiensis* (*1*, *7*), but some argue that it is a pathological modern human (*4*, *6*). Here we examine the morphology of three wrist bones attributed to LB1 to test these competing hypotheses.

Wrist morphology can be a powerful indicator of phylogenetic relationships in Mammalia because of variation in the number and shape of carpal elements and in the configuration of the articular surfaces (*8*–*12*). In primates, the trapezoid is the wrist bone situated directly proximal to the index finger. The modern human trapezoid is shaped like a boot (*9*, *13*, *14*), wherein the palmar half of the bone is radio-ulnarly and proximo-distally wide (Fig. 1). In contrast, other primates have a trapezoid that is more wedge-shaped with a narrow palmar tip and a wide dorsal base (*9*, *13*–*15*). This difference between human and nonhuman primate trapezoid shape is concomitantly reflected by the shapes and articular configurations of the carpals that articulate with the trapezoid, and all of these carpals are derived in modern humans in comparison to those in other primates (Figs. 2 and 3) (*9*, *13*). Upper Paleolithic *Homo sapiens* and Neandertals share these derived morphological features with modern humans, suggesting that they are most likely inherited from a recent common ancestor (*13*). A capitate attributed to *Homo antecessor* (*16*) and dated to ~0.8 million years ago (Ma) (*17*) also shares the derived condition (*13*, *16*). Thus, the current paleontological evidence suggests that this complex of wrist features evolved by at least 800,000 years ago.

Three complete carpals—a trapezoid, scaphoid, and capitate—all of which are from a left wrist, were recovered along with the cranium, mandible, and additional postcranial material of LB1 in Spit No. 59 of Sector VII during the September 2003 excavation (fig. S1 and table S3) (*1*, *2*, *18*). Each is well preserved and shows no signs of pathology or abnormal development. As shown in Figs. 1 to 3, these three articulating bones display none of the shared, derived features of modern human and Neandertal carpals (*13*). Instead, they show the general symplesiomorphic pattern exhibited by all extant African apes, as well as fossil hominins that preserve comparable wrist morphology and date before 1.7 Ma (*13*, *19*–*22*). Like other nonhuman primates, LB1's trapezoid is (i) wedge-shaped; (ii) the ulnar side of its second metacarpal articulation is oriented more sagittally (Fig. 1, top and bottom rows); (iii) its scaphoid articular surface is more triangular in shape (Fig. 1, middle row); and (iv) it lacks the expanded palmar nonarticular area (Fig. 1, top row) and the more palmarly placed capitate articulation observed in modern humans and Neandertals (Fig. 1, bottom row). We quantified these shape differences using three-dimensional (3D) methods measuring the relative areas and angles of carpal articular surfaces (*13*, *14*, *18*, *23*). Multivariate statistical analysis of these data distinguishes modern humans and Neandertals from the great apes, *Papio*, and LB1 (Fig. 1). Primarily, the trapezoids of modern humans and Neandertals are distinct in their shape and articular configuration as a consequence of the large expansion of palmar nonarticular area, which tends to square off the entire palmar half of the bone (Fig. 1, top row) (*13*).

The scaphoid and capitate of LB1 both exhibit the shapes and articular configurations that occur concomitantly with the primitive hominid trapezoid condition (*13*, *18*), and multivariate analyses of these carpals provide similar results (Figs. 2 and 3). For example, LB1's capitate lacks the enlarged palmarly placed articular surface for the trapezoid observed in modern humans and Neandertals (*9*, *13*) and, instead, shows the waisted neck characteristic of extant

[1]Human Origins Program, Department of Anthropology, National Museum of Natural History, Smithsonian Institution, Washington, DC 20013, USA. [2]School of Human Evolution and Social Change, Arizona State University, AZ 85287, USA. [3]Institute of Human Origins, Arizona State University, AZ 85287, USA. [4]Department of Anatomical Sciences, School of Medicine, Stony Brook University, NY 11794, USA. [5]The National Research and Development Centre for Archaeology, Jakarta, Indonesia. [6]School of Earth and Environmental Sciences, University of Wollongong, NSW 2522, Australia.

*To whom correspondence should be addressed. E-mail: tocherim@si.edu